High electronic conductivity as the origin of lithium dendrite formation within solid electrolytes

Fudong Han[1], Andrew S. Westover[2], Jie Yue[1], Xiulin Fan[1], Fei Wang [ID][1], Miaofang Chi [ID][3], Donovan N. Leonard[2], Nancy J. Dudney [ID][2]*, Howard Wang [ID][4]* and Chunsheng Wang [ID][1]*

Solid electrolytes (SEs) are widely considered as an 'enabler' of lithium anodes for high-energy batteries. However, recent reports demonstrate that the Li dendrite formation in $Li_7La_3Zr_2O_{12}$ (LLZO) and $Li_2S–P_2S_5$ is actually much easier than that in liquid electrolytes of lithium batteries, by mechanisms that remain elusive. Here we illustrate the origin of the dendrite formation by monitoring the dynamic evolution of Li concentration profiles in three popular but representative SEs (LiPON, LLZO and amorphous Li_3PS_4) during lithium plating using time-resolved operando neutron depth profiling. Although no apparent changes in the lithium concentration in LiPON can be observed, we visualize the direct deposition of Li inside the bulk LLZO and Li_3PS_4. Our findings suggest the high electronic conductivity of LLZO and Li_3PS_4 is mostly responsible for dendrite formation in these SEs. Lowering the electronic conductivity, rather than further increasing the ionic conductivity of SEs, is therefore critical for the success of all-solid-state Li batteries.

Lithium metal is being considered as the ultimate goal for the anode of a high-energy rechargeable battery[1], but use of Li anodes with traditional liquid or polymer electrolytes has not been successful due to difficulties in suppressing dendrite formation[2–4]. Solid electrolytes (SEs) are believed to be able to prevent Li dendrite growth because of their high mechanical strength and high Li+ transference number[5–8], as demonstrated by thousands of cycles of LiPON-based thin-film Li batteries even at current densities as high as $10 \, mA \, cm^{-2}$ (refs. [9,10]). However, the low ionic conductivity of LiPON restricts its application solely to thin-film batteries that have limited capacity, and therefore integrating lithium anodes with highly conductive SEs ($>10^{-4} \, S \, cm^{-1}$) is required to develop a high-energy bulk-type all-solid-state lithium battery[5].

Significant advances have been achieved in developing superionic SEs with ionic conductivities approaching or even surpassing those of liquid electrolytes[11–13]. Among them, $Li_7La_3Zr_2O_{12}$ (LLZO) and $Li_2S–P_2S_5$ are considered the most promising SEs to be used with Li metal anodes because of their excellent compatibility with Li[12,14]. However, recent reports have indicated that lithium dendrites form in LLZOs, regardless of the dopants used for stabilizing the cubic structure[14–26], and also in $Li_2S–P_2S_5$ SEs, including $70Li_2S–30P_2S_5$ glass[26], $75Li_2S–25P_2S_5$ glass[27,28], $80Li_2S–20P_2S_5$ glass ceramic[29] and polycrystalline $β-Li_3PS_4$[26]. The formation of dendrites leads to short circuiting of the Li/LLZO/Li or $Li/Li_2S–P_2S_5/Li$ cells at large currents. The critical current density, at which the cell will be shorted, is less than $0.9 \, mA \, cm^{-2}$ for LLZO and $1.0 \, mA \, cm^{-2}$ for Li_3PS_4 at room temperature[14,17,20,22,24,27,28,30], whereas the critical current density of liquid electrolytes can reach $4–10 \, mA \, cm^{-2}$ at room temperature[31,32]. A detailed comparison of the properties of these electrolytes is listed in Supplementary Table 1. These results indicate that dendrite formation in LLZO and $Li_2S–P_2S_5$ SEs is actually much easier than that in liquid-electrolyte lithium cells, contradicting the conventional understanding of dendrites that they can be prevented if the electrolytes have a Li transference number close to 1.0[7] or shear modulus larger than twice that of Li[6]. Knowledge about such an unexpected behaviour remains insufficient.

Lithium dendrites tend to grow along the grain boundaries and voids in SEs[21,29]. The low relative density of SEs was believed to be the major reason for Li dendrite growth, but there is no correlation between dendrite suppression and the relative density of LLZO[20]. In fact, Li dendrites still grow in a very dense LLZO (relative density >97%)[20–22]. The low lithium ion diffusivity at the grain boundaries was also reported to be the reason for the dendrite formation[15,16,33]. However, increasing the ionic conductivity of grain boundaries cannot effectively improve the capability for dendrite suppression[15,16]. Pre-existing defects in surface and bulk SEs, such as cracks, were also thought to be the primary reason for dendrite growth[8,26], because the growth of dendrites in defects/cracks will be easier and the generated stress can further extend the crack, promoting Li dendrite propagation. However, this theory cannot fully explain why the dendrites form at a similar current density in LLZO with different surface roughness and why the dendrites still form in single-crystalline LLZO[26]. Inhomogeneous lithium plating due to insufficient interfacial contact between Li and SEs has also been considered as the reason for the dendrite formation, as the critical current density increases with the decrease in interfacial resistance between Li and SEs[14,17,20,25,28]. However, the dendrites still form at a low current density ($<0.9–1 \, mA \, cm^{-2}$) even if the area specific resistance (ASR) of the Li/electrolyte interface has been optimized to be comparable to or even lower than that in the liquid-electrolyte or LiPON-based lithium cells[14,17,25]. Until now there has been no theory that can reconcile all these inconsistencies, and there is no clear route to prevent

[1]Department of Chemical and Biomolecular Engineering, University of Maryland, College Park, MD, USA. [2]Materials Science and Technology Division, Oak Ridge National Laboratory, Oak Ridge, TN, USA. [3]Center for Nanophase Materials Sciences, Oak Ridge National Laboratory, Oak Ridge, TN, USA. [4]Department of Materials Science and Engineering, University of Maryland, College Park, MD, USA. *e-mail: dudneynj@ornl.gov; wangh@umd.edu; cswang@umd.edu

lithium dendrite formation in LLZO and $Li_2S–P_2S_5$ SEs at the current density ($10\,mA\,cm^{-2}$) required for the fast-charge goal[4], which may prevent their successful integration with lithium anodes.

Here, we use operando neutron depth profiling (NDP) to investigate the mechanisms of dendrite formation in LLZO and Li_3PS_4. By monitoring the dynamic evolution of the lithium concentration profiles in the SEs of $LiCoO_2$/LiPON/Cu, Li/LLZO/Cu and Li/Li_3PS_4/Pt cells during Li plating, we visualized that Li dendrites can directly deposit inside LLZO and Li_3PS_4 SEs, whereas no dendrite formation can be observed in LiPON. The direct formation of dendrites inside LLZO and Li_3PS_4 suggests that high electronic conductivity is probably the root cause for dendrite formation in these SEs.

Features of dendrites formed by electronic conduction

The distinct difference between LLZO, $Li_2S–P_2S_5$ and LiPON in Li dendrite suppression motivates us to carefully consider what properties differentiate these electrolytes. First, we compare LLZO with LiPON (Supplementary Table 1). The relative density of a well-prepared LLZO electrolyte is similar to that of LiPON. The shear modulus of LLZO is about twice that of LiPON[34]. The ASR of the Li/LLZO interface can be much lower than that of the Li/LiPON interface[25,35]. Moreover, the ionic conductivity of LLZO ($10^{-4}\,S\,cm^{-1}$) is much higher than that of LiPON ($10^{-6}\,S\,cm^{-1}$). All of these properties should ensure that LLZO has a similar (if not higher) dendrite suppression capability to that of LiPON. Therefore, there must be other properties that govern the dendrite growth. Interestingly, the critical current density of SEs seems to correlate well with their electronic conductivities (Supplementary Table 1). The electronic conductivities of LLZO ($10^{-8}–10^{-7}\,S\,cm^{-1}$)[36,37] and $Li_2S–P_2S_5$ ($10^{-9}–10^{-8}\,S\,cm^{-1}$)[38,39] are several orders of magnitude higher than that of LiPON ($10^{-15}–10^{-12}\,S\,cm^{-1}$)[40–42], whereas the critical current densities of LLZO ($0.05–0.9\,mA\,cm^{-2}$)[14,17,20,24,25] and $Li_2S–P_2S_5$ ($0.4–1\,mA\,cm^{-2}$)[27,28] are much lower than that of LiPON ($>10\,mA\,cm^{-2}$)[9]. It should be noted that the electronic conductivity of LLZO and $Li_2S–P_2S_5$ may be further enhanced during Li plating because some of the impurities/dopants and the SEs themselves may be reduced at the Li plating potential ($<0\,V$ versus Li/Li^+)[28,36,43]. A recent study shows that the electronic conductivity of LLZO can increase from $1.2\times10^{-7}\,S\,cm^{-1}$ to $1.1\times10^{-6}\,S\,cm^{-1}$ after LLZO is reduced[36]. The high electronic conductivities of LLZO and $Li_2S–P_2S_5$ allow Li^+ to combine with electrons to form lithium dendrites directly inside these SEs when the potential reaches the Li-plating potential. Similar phenomena were also reported in sodium solid electrolytes. It has been reported that the enhanced electronic conduction in sodium β-alumina can lead to the deposition of sodium metal directly inside the electrolyte[44,45]. Moreover, isolated Li nuclei can also form inside the solid electrolyte interphase (SEI), formed from reduction of liquid-electrolyte in lithium metal batteries, when the electronic conductivity of the SEI is high[46,47]. The high electronic conductivity of LLZO and $Li_2S–P_2S_5$ could potentially be the primary reason for the dendrite formation in these SEs, but have never been considered in previous research efforts. Testing this hypothesis is particularly important since most current research on SEs is focused on improving the ionic conductivity with various strategies (for example, doping), although these strategies may increase the electronic conductivity. The findings are critical for determining the future research focus of SEs.

Unlike conventional interface-controlled dendrite growth wherein the dendrites grow only from lithium anode to cathode[3], the distinct feature of electronic-conduction-induced dendrite formation is that Li dendrites can deposit directly inside the SE. Specifically, in the conventional lithium growth mechanism, Li dendrites are interconnected and the amount of Li tends to decrease with increasing distance from the anode/electrolyte interface (perpendicular to the interface). In contrast, Li deposition induced by electronic conduction forms dendrites that are isolated and the

amount of Li plated in this way is not sensitive to the distance from the anode/electrolyte interface. Therefore, tracking the Li distribution throughout a SE perpendicular to the anode/electrolyte interface during Li plating will give direct mechanistic insights into dendrite formation in SEs.

Time-resolved lithium concentration profiles

Neutron depth profiling (NDP), a non-destructive neutron analytical technique[48,49], is used here to determine the dynamic evolution of the lithium concentration profiles in the SEs of $LiCoO_2$/LiPON/Cu, Li/LLZO/Cu and Li/Li_3PS_4/Pt cells during Li plating. $LiCoO_2$ instead of Li metal is used as the lithium source for the cell based on LiPON because LiPON as a thin film cannot be readily deposited on Li foil. Polycrystalline LLZO is used to make the Li/LLZO/Cu cells. Amorphous Li_3PS_4 (or $75Li_2S–25P_2S_5$ glass) is used as a model material for $Li_2S–P_2S_5$ SEs. Figure 1a shows the schematic set-up of the operando NDP experiment. The NDP measurement was performed on NG5 at the NIST NCNR. The cell structures with different SEs are shown in Fig. 1b. Li is plated on the Cu or Pt, during which a real-time NDP profile is measured from the top surfaces of these cells.

Figure 1c–e depicts snapshots of the lithium concentration profiles in these three SEs during lithium plating. Detailed data analysis of the NDP profiles can be found in the Supplementary Figs. 1–3 and Supplementary Table 2. The '0 μm' on the depth scale is defined as the interface between Cu (or Pt) and the SE prior to Li plating. Positive depth values encompass the thickness of SEs. The results indicate that almost all the 3.2-μm-thick LiPON electrolyte could be measured, whereas the measurable depths of LLZO and Li_3PS_4 are 16 μm and 24 μm, respectively, which are thinner than the overall thickness of these two electrolytes (1 mm). All the profiles are divided into a surface region and a bulk region by the depth at which the tail of the Li peak disappears. The surface region includes the Cu (or Pt), the deposited Li and part of the SE, whereas the bulk region refers to the bulk of the SE only. The gradual increase of the peaks in the surface region indicates the continuous plating of Li on the anode.

In this work, Li was plated only in one direction, to exclude any complications from the 'dead lithium' generated due to the incomplete dissolution of lithium during Li stripping. Figure 2a shows the voltage profile of the $LiCoO_2$/LiPON/Cu cell for the first charge process (Li plating on Cu) at a step-increased current density at 25 °C (Fig. 2a). Typical impedance spectra for a $LiCoO_2$/LiPON/Cu cell were obtained before and after Li plating (Supplementary Fig. 4a). No short circuit was observed from the voltage profile and impedance of the $LiCoO_2$/LiPON/Cu cell. On the other hand, the voltages of the Li/LLZO/Cu (Fig. 2b,c) and the Li/Li_3PS_4/Pt (Fig. 2e,f) cells during discharging (Li plating on Cu or Pt) at 25 °C and 60 °C quickly decreased to negative values at step-increased currents, and then increased to around 0 V due to shorting of these cells. The shorting was also confirmed by the impedance spectra (Supplementary Fig. 4). The critical current densities of the Li/LLZO/Cu and Li/Li_3PS_4/Pt cells at 25 °C are $50\,\mu A\,cm^{-2}$ and $120\,\mu A\,cm^{-2}$, respectively, consistent with previous reports[14,28].

Interestingly, when the Li/LLZO/Cu cell was discharged at 100 °C at a step-increased current up to $1.06\,mA\,cm^{-2}$, the voltage of the Li/LLZO/Cu cell gradually decreased to $-4.0\,V$ (versus Li counter electrode) and then rapidly dropped to $-7.0\,V$ after the last step increase in the current (Fig. 2d). The test was terminated at 29,880 s with a cumulative charge of $4.6\,mAh\,cm^{-2}$, apparently without shorting. The rapid voltage drop to $-7\,V$ at large currents was also observed from the Li/Li_3PS_4/Pt cell tested at 100 °C at $2\,mA\,cm^{-2}$ with a cumulative charge of $1.2\,mAh\,cm^{-2}$ (Fig. 2g). The current–voltage behaviours of Li/LLZO/Cu and Li/Li_3PS_4/Pt cells discharged at 100 °C are reproduced with two other batteries, and all the voltage behaviours are consistent with the results reported by Tsai[20]. Tsai attributed this abnormal voltage behaviour to loss of
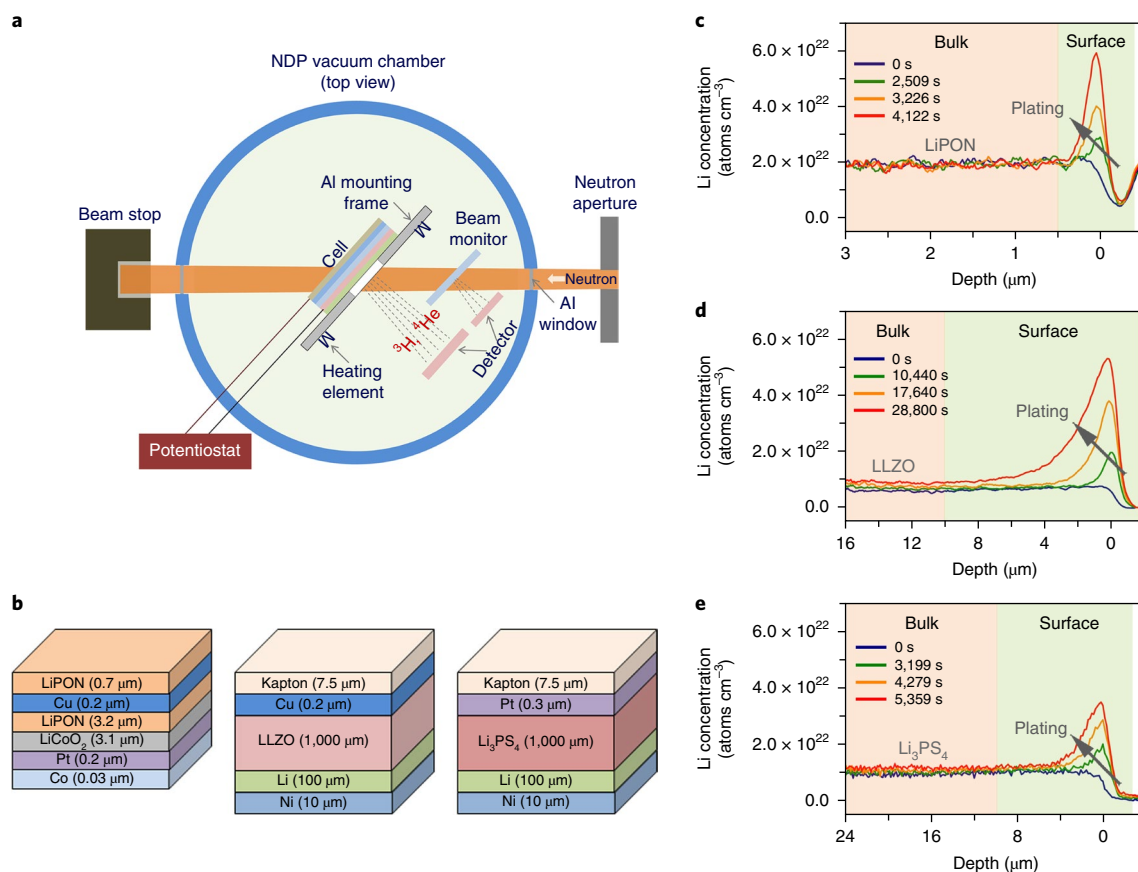
Fig. 1 | Operando NDP. a, Schematic of the experimental set-up for operando NDP. **b,** Schematic structures of LiCoO$_2$/LiPON/Cu, Li/LLZO/Cu and Li/Li$_3$PS$_4$/Pt cells. Li is plated on Cu or Pt, and the depth profiles are measured from the top surfaces of the cells during plating. **c–e,** Time-resolved lithium concentration profiles for LiCoO$_2$/LiPON/Cu (**c**), Li/LLZO/Cu (**d**) and Li/Li$_3$PS$_4$/Pt (**e**) cells. The lithium concentration profiles in **d** and **e** are obtained from cells tested at 100 °C. The grey arrows indicate continous plating of Li.

contact between LLZO and the Li counter electrode, as the Li is dissolved from the Li/LLZO interface, leading to an increase in the interface resistance between LLZO and Li. The contact loss agrees with the increase in the voltage of the Li counter electrode measured by a three-electrode test (Supplementary Fig. 5g), and is also consistent with the greatly increased interfacial resistances of the cells after discharge (Supplementary Figs. 4d, g). We speculate the loss of the Li contact may prevent complete short-circuiting of the cell because it leads to a highly positive potential at the Li counter electrode (Supplementary Fig. 5g). The large amount of Li transported from the Li counter electrode without shorting allowed us to map the Li distribution in LLZO and Li$_3$PS$_4$ over a long-period Li plating at high currents.

Correlation between electric charge and accumulated Li

We first quantified the net amount of Li transported from the counter electrode (LiCoO$_2$ or Li) by integrating the counts in all the measurable depths, including the surface region and bulk region of the cells (named 'total region'), and subtracting the initial counts measured prior to the application of current. The amount of Li transported from the counter electrode (LiCoO$_2$ or Li) was then compared with the cumulative electric charge.

Figure 3a shows that the amount of Li in the total region of the LiCoO$_2$/LiPON/Cu cell increases during the initial charge, and the accumulated amount of Li correlates well with the cumulative charge. On the other hand, no obvious increase in the amount of Li in the total region can be observed in the Li/LLZO/Cu and Li/Li$_3$PS$_4$/Pt cells tested at 25 °C (Fig. 3b,e) because the cumulative

charge before shorting is too low and therefore the amount of Li transported can hardly be detected by NDP. Increasing the test temperature to 60 °C led to a larger amount of Li transported from the Li counter electrode in the Li/LLZO/Cu cell (Fig. 3c) and Li/Li$_3$PS$_4$/Pt cell (Fig. 3f). The amount of accumulated Li correlates well with the cumulative charge at the beginning of the measurement, and then deviates after a certain amount of time for both cells. The deviation suggests that the amount of Li transported to the total region is less than the cumulative charge, suggesting that the dendrites have formed in the deep, undetectable region of the SEs. It should be noted that the enhanced electronic conductivity of SEs from their reduction (under the Li plating potential)[36,43] or from the formed dendrites may also contribute slightly to the deviation. The deviation further increases after the test temperature was increased to 100 °C (Fig. 3d,g), demonstrating that a large number of dendrites have been formed in the SEs, albeit without short-circuiting the cells tested at 100 °C (Fig. 2d,g). The formation of dendrites in LLZO and Li$_3$PS$_4$ after testing at 100 °C is also confirmed from the microscopic characterization of these SEs (Supplementary Figs. 6,7).

We then quantified the lithium content in the bulk regions of the SE in each of the cells. The SEs were denoted as LiPON-25 °C, LLZO-25 °C, LLZO-60 °C, LLZO-100 °C, Li$_3$PS$_4$-25 °C, Li$_3$PS$_4$-60 °C and Li$_3$PS$_4$-100 °C based on the testing temperature used for Li plating. The lithium content in the bulk region of LiPON-25 °C remains constant during the entire lithium plating process (Fig. 4), indicating that the Li accumulation in the total region (Fig. 3a) is attributed only to the Li plating on Cu. The excellent correlation
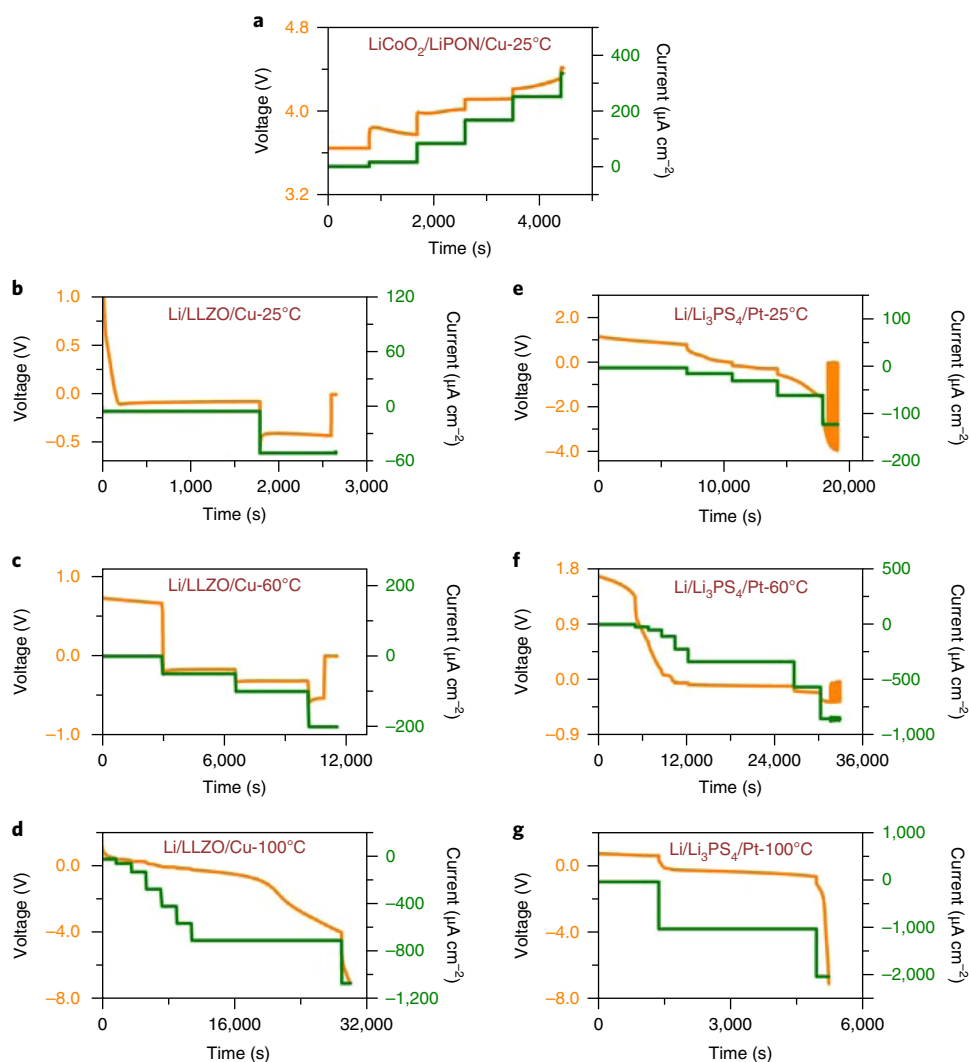
Fig. 2 | Electrochemistry. a, Voltage–time curve for the initial charge of the LiCoO$_2$/LiPON/Cu cell with the magnitude of the current density increased step-wise at 25 °C. **b–d**, Voltage–time curves of the Li/LLZO/Cu cells discharged with the magnitude of the current density increased step-wise at 25 °C (**b**), 60 °C (**c**) and 100 °C (**d**). **e–g**, Voltage–time curves of the Li/Li$_3$PS$_4$/Pt cells discharged with the magnitude of the current density increased step-wiseat 25 °C (**e**), 60 °C (**f**) and 100 °C (**g**).

between the amount of Li deposited on Cu and the cumulative charge indicate that no dendrites were formed in bulk LiPON, consistent with the electrochemical results (Fig. 2a). No apparent change of the Li content can be detected in the bulk regions of LLZO-25 °C and Li$_3$PS$_4$-25 °C, indicating that shorting of the Li/LLZO/Cu and Li/Li$_3$PS$_4$/Pt cells at 25 °C is caused by rapid formation of very thin dendrites whose net Li content is below the detection limit of NDP. However, the lithium contents in the bulk regions of LLZO-60 °C and Li$_3$PS$_4$-60 °C increase from $t/t_0 = 0.4$ (real time of 4,581 s) and $t/t_0 = 0.5$ (real time of 16,550 s), respectively. The results confirmed dendrite formation in both LLZO-60 °C and Li$_3$PS$_4$-60 °C and, more importantly, showed that the formation of dendrites occurs much earlier than the shorting can be observed from the voltage profile (Fig. 2c,f), consistent with previous result from an in-situ acoustic study[19]. The lithium contents in the bulk regions of LLZO-100 °C and Li$_3$PS$_4$-100 °C start to increase at around $t/t_0 = 0.3$, and keep increasing until the termination of the test, indicating the dendrites form continuously in these SEs during Li plating. The content of Li dendrites formed at 100 °C is much higher than that formed at 60 °C for both electrolytes, consistent with the results shown in Fig. 3.

Dendrite distribution inside SEs

To understand how the dendrites grow in LLZO and Li$_3$PS$_4$, the evolution of detailed lithium concentration profiles in LiPON, LLZO and Li$_3$PS$_4$ SEs during lithium plating were analysed (Fig. 5a–g). As expected, the lithium distribution in the bulk LiPON-25 °C is uniform and remains unchanged during the entire lithium plating process (Fig. 5a). No obvious change can be observed in the lithium concentration profiles of the bulk LLZO-25 °C (Fig. 5b) and Li$_3$PS$_4$-25 °C (Fig. 5e) due to the limited amount of dendrites formed. On the other hand, the increased lithium content in the bulk LLZO-60 °C and Li$_3$PS$_4$-60 °C can be observed from Fig. 5c,f and, more importantly, the accumulated contents of Li in these SEs seem to be irrelevant to depth. A clearer evolution can be observed from the lithium concentration profiles of LLZO-100 °C (Fig. 5d) and Li$_3$PS$_4$-100 °C (Fig. 5g). It was shown that the lithium contents at different depths of LLZO-100 °C and Li$_3$PS$_4$-100 °C increase uniformly during Li plating (Fig. 5d,g). These results cannot be explained by the conventional understanding of directional dendrite growth[3], which predicts the existence of a lithium concentration gradient in the front of the dendrite region (towards the cathode) (Supplementary Fig. 8a), regardless of the growth modes of dendrites (tip, root, or
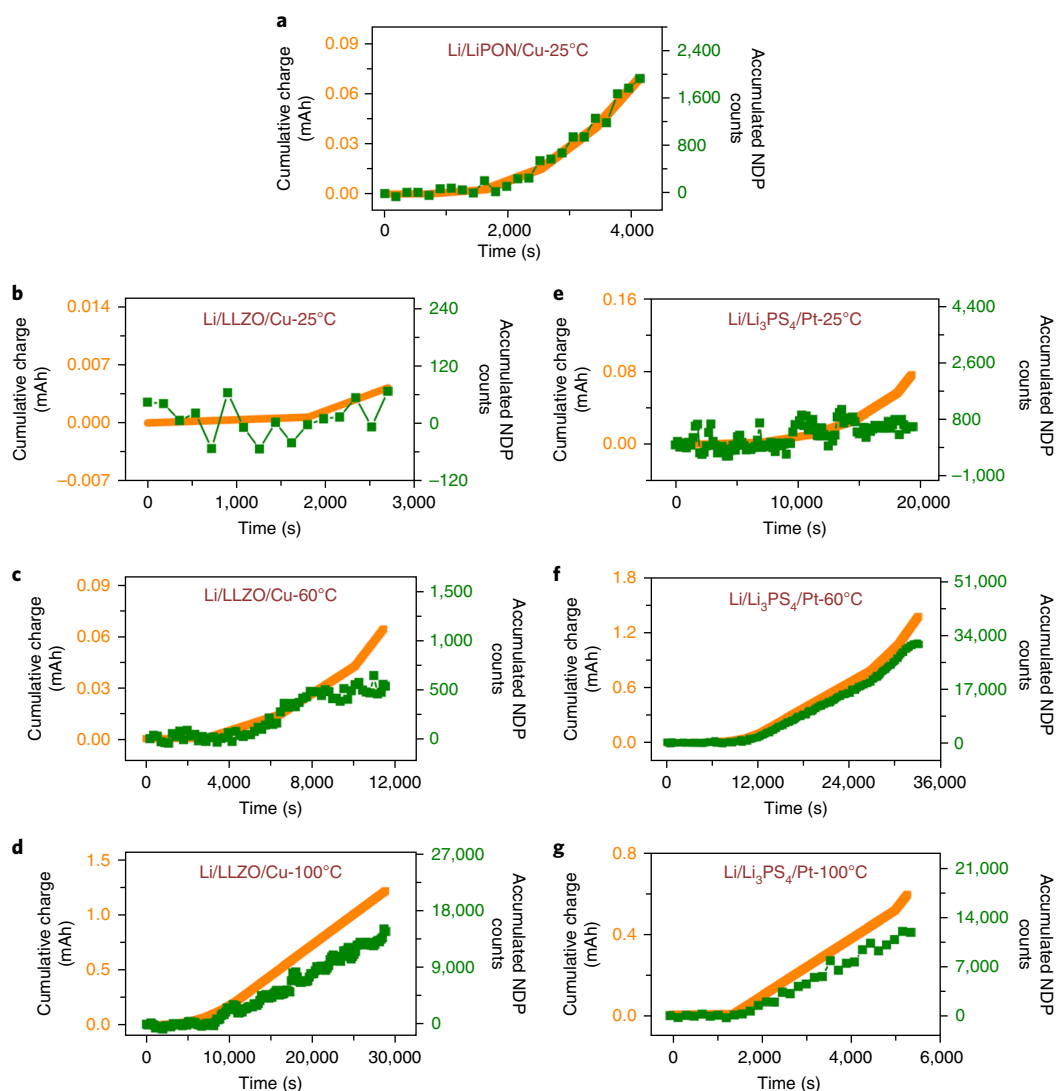
Fig. 3 | Correlation between electric charge and accumulated Li content. a–g, Correlations between cumulative charges (orange line) and the accumulated NDP counts (green dots) in the total region (surface and bulk) of the $LiCoO_2/LiPON/Cu$ cell (**a**), the Li/LLZO/Cu cells tested at 25 °C (**b**), 60 °C (**c**) and 100 °C (**d**), and the $Li/Li_3PS_4/Pt$ cells tested at 25 °C (**e**), 60 °C (**f**) and 100 °C (**g**).

tortuous growth). Instead, the uniform increase of dendrite content across the measurable thickness of the SEs can be caused only by the direct deposition of dendrites inside the bulk region of LLZO and Li_3PS_4 (Supplementary Fig. 8b).

Given that the lithium concentration profiles were collected over a large area (>0.3 cm²) of the LLZO and Li_3PS_4, these results reflect the true evolution of the lithium distribution in these SEs. The direct nucleation and growth of dendrites inside LLZO is also supported by focused ion beam–scanning electron microscope (FIB-SEM) images with a 60 nm per step sectioning (Supplementary Fig. 9 and Supplementary Video 1). In these images, no apparent interconnections were observed between the black spots (Li dendrites) inside LLZO, although more careful characterizations with a higher spatial resolution are still required to be more conclusive. It should be noted that the Li dendrites are only randomly formed at some places in the SE pellets, as shown in previous work[18,20,23,28] and in our results (Supplementary Figs. 6, 7 and 9), and until now there has been no direct proof that the dispersed dendrites formed in the SEs are interconnected. The direct formation of isolated dendrites inside SEs can also explain why the response from the voltage profile lags far behind the initiation of dendrites.

The direct nucleation and growth of dendrites inside LLZO and Li_3PS_4 suggest that dendrite formation in these SEs is caused by the electronic conductivity of these electrolytes. A possible mechanism for the dendrite formation is proposed on the basis of the experimentally observed results. Two critical conditions have to be satisfied simultaneously for lithium dendrites to be deposited inside a SE: the presence of mobile electrons in the electrolyte (indicated by the electronic conductivity), and the potential in the electrolyte below the Li plating potential (<0 V versus Li/Li⁺). The overpotential must provide a sufficient driving force for the nucleation and growth of dendrites in the SEs. A simplified electro-chemo-mechanical model has been developed to quantify the driving force for dendrite formation inside SEs[33]. On the basis of this model, the critical potential is calculated to be −17 to −27 mV if the fracture stress of the SE is between 30 and 100 Mpa. It is known that the potential in the bulk electrolyte is determined by the electrochemical potential of Li⁺ and the electrochemical potential of electrons[50]. Therefore, a higher electronic conductivity of the electrolyte will result in a lower potential in the bulk electrolyte, which will provide a larger driving force for dendrite formation.
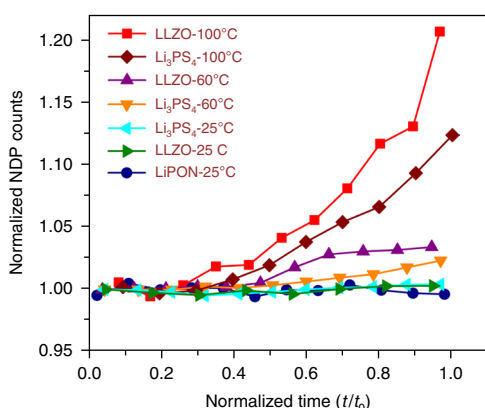
Fig. 4 | Evolution of the Li content of dendrites in the bulk region of SEs. The normalized NDP count, shown on the y axis, is the ratio of the measured count to the initial count (before Li plating) in the bulk regions of SEs, and the normalized time, t/t_0, shown on the x axis, is the ratio of the real time t to the total time t_0 of the test (the total times are 4,453 s for the LiCoO$_2$/LiPON/Cu cell, 2,703 s for the Li/LLZO/Cu cell tested at 25 °C, 11,454 s for the Li/LLZO/Cu cell tested at 60 °C, 29,880 s for the Li/LLZO/Cu cell tested at 100 °C, 19,190 s for the Li/Li$_3$PS$_4$/Pt cell tested at 25 °C, 33,099 s for the Li/Li$_3$PS$_4$/Pt cell tested at 60 °C, and 5,290 s for the Li/Li$_3$PS$_4$/Pt cell tested at 100 °C). The data were smoothed across adjacent points using the Savitky–Golay algorithm.

It should be noted that a potential gradient is expected in the LLZO and Li$_3$PS$_4$ SEs because of electronic conduction. However, unlike the large potential gradient in liquid-electrolyte batteries, where both cations and anions are mobile, the potential gradient should be extremely small, based on the high Li-ion transference number close to 1.0 (refs. [51,52]). On the other hand, the potential at local positions in the SE can fluctuate widely, based on the large microstructural and/or compositional heterogeneities in SEs[53,54], especially at defects such as impurities, grain/particle boundaries and voids. At these local positions, the electronic conductivity can be higher or the fracture stress can be lower, both of which can lower the driving forces (or local critical overpotential) for dendrite formation. We believe potential fluctuations due to these heterogeneities can easily surpass the potential gradient caused by electronic conduction, leading to the formation of dendrites at dispersed locations, instead of a directional propagation of dendrites, across the thickness of the SEs. These local positions with a lower critical potential would be expected to be statistically distributed within the entire solid electrolyte pellet, and therefore a nearly uniform distribution of dendrites can be detected from NDP measurements with a detected area > 0.3 cm^2 (Fig. 5d,g), although microscopically speaking the dendrites are not uniformly distributed in the SEM images (Supplementary Figs. 6, 7 and 9) with detected areas around hundreds of square micrometres. The nucleation and growth of dendrites within the SE could further increase the electronic conductivity of the SE[36], which would promote the continuous deposition of dendrites until they are connected to form a metallic percolation, leading to shorting of the cell.

Electronic conductivity measurement

To corroborate the proposed mechanism, the electronic conductivities of LLZO and Li$_3$PS$_4$ SEs at different temperatures were also measured. Figure 6a,c shows the current–time curves of the Cu/LLZO/Cu and Cu/Li$_3$PS$_4$/Cu cells under DC polarization at 100 mV at different temperatures. By applying a constant voltage, the current first decreases and then reaches a steady state. At the steady state, the current is attributed only to electronic leakage, since two ion-blocking Cu electrodes were used. The electronic conductivities determined

by this approach are shown in Fig. 6b,d. The electronic conductivities of LLZO and Li$_3$PS$_4$ at 30 °C are 5.5×10^{-8} and 2.2×10^{-9} S cm^{-1}, respectively, which agrees with previous reports[37–39]. These values are much lower than the electronic conductivity of LiPON (10^{-15}–10^{-12} S cm^{-1})[40–42] measured by two ion-blocking electrodes. More importantly, the electronic conductivities of both electrolytes increase with temperature. It should be noted that the electronic conductivity measurement using two ion-blocking electrodes is not the same as a real Wagner–Hebb measurement using a Li electrode and an ion-blocking electrode, but instead provides an upper limit of the electronic conductivity[42]. The Wagner–Hebb method was not used to obtain the electronic conductivities of Li$_3$PS$_4$ and LLZO because neither of these electrolytes is thermodynamically stable against Li metal[5,38,43]. Even slight decomposition of the SEs will lead to a noticeable influence on the measurement and data analysis (Supplementary Fig. 10). Nonetheless, the increase in electronic conductivity with temperature (Fig. 6) is consistent with the proposed mechanism, as the dendrite content also increases with increasing temperature.

Discussion

It is worth noting that, as an intrinsic property of SEs, the capability for Li dendrite suppression should be described by the magnitude of the critical overpotential inside the SE. Since the precise measurement of the potential in the SE is difficult, the critical current density is used as a compromise to evaluate the capability for dendrite suppression of electrolytes[14,17,20,28] assuming that the ASR of the cell is the same. However, the critical current density cannot represent the capability for dendrite suppression if the SEs are tested under remarkably different experimental conditions, such as different electrode geometries (three-dimensional versus planar), different capacities or different temperatures. Under these distinct conditions, the ASR of the cell will change noticeably. For example, at a higher temperature, the electronic and ionic conductivities of the SE will increase and the interfacial resistances will decrease, all of which will lead to a decreased overpotential in the SE at the same current density. Therefore, the higher critical current density at a higher temperature is simply a result of improved kinetics, rather than improved capability for dendrite suppression. For electrolytes tested under remarkably different experimental conditions, we provide an alternative approach to evaluate their capability to suppress dendrite formation by measuring the potential of the anode in a three-electrode cell. As can be seen in Supplementary Fig. 5, the high potential of the Li/LLZO/Cu cells is mainly attributed to the potential gradient at the cathode/electrolyte interface, while the overpotential of the Cu anode decreases from 22.6 to 5.1 mV when the temperature increases from 25 to 100 °C. The results indicate that a lower driving force is needed for dendrite formation at a higher temperature, which agrees well with the proposed mechanism, as the electronic conductivity is increased at a higher temperature.

Although it is not the main focus of the present work, we still cannot fully understand why more dendrites are needed to completely short the cell at a higher temperature. One possible reason would be thermal relaxation of the dendrites, as it has been suggested that a higher mobility of Li atoms at a higher temperature can help reduce the surface area of the dendrites and promote isotropic lithium growth[55,56]. In other words, the Li nuclei deposited inside the SE tend to grow towards a spherical morphology instead of a needle-like morphology at a higher temperature, and therefore a larger amount of dendrites are needed to form the metallic percolation to short the battery. Nonetheless, more careful characterizations with a higher spatial resolution on multiple dendrites formed at different temperatures are needed to confirm this hypothesis.

The proposed electronic-conduction-induced dendrite formation mechanism helps to reconcile the inconsistent results from previous studies. Improving the relative density of LLZO may
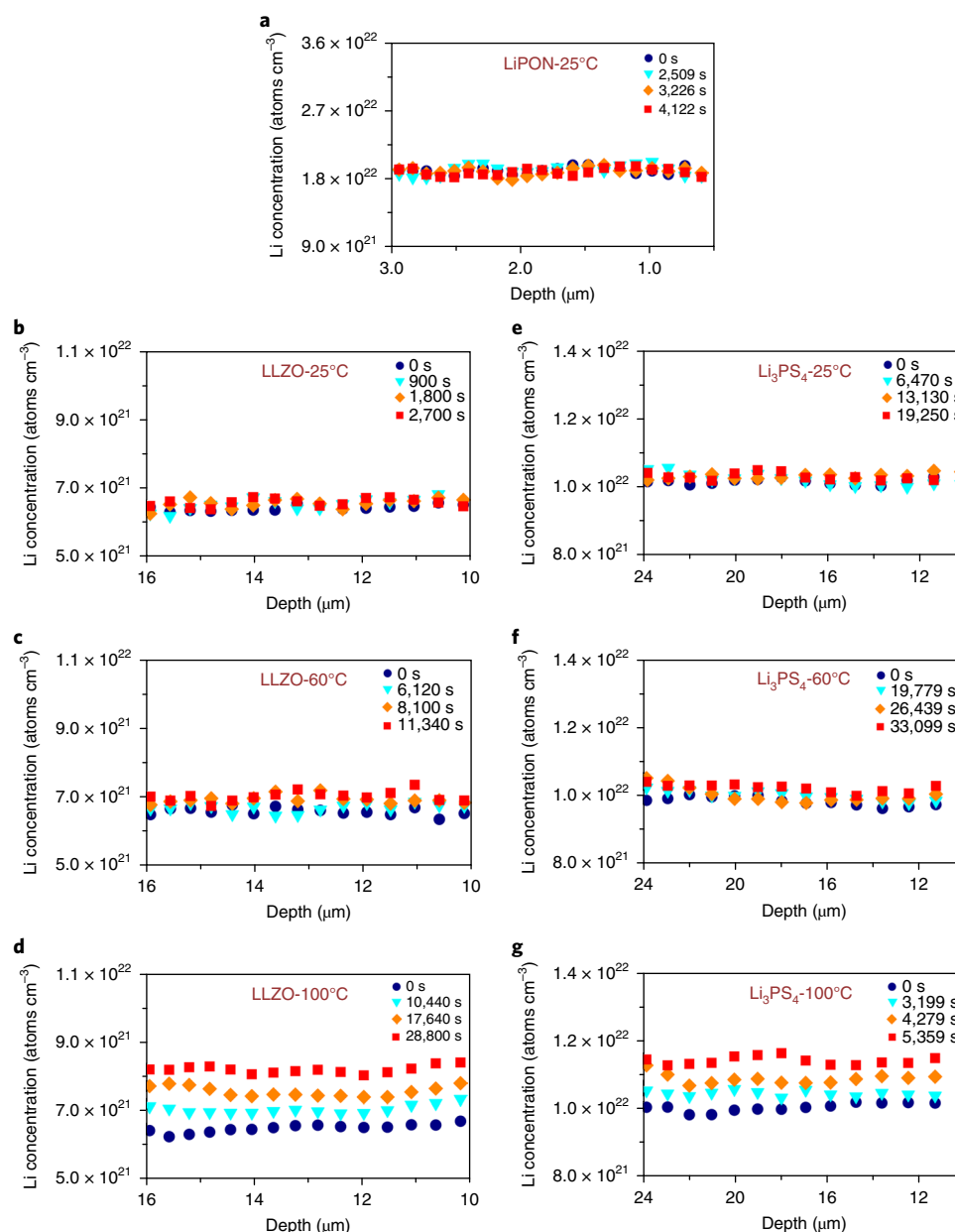
Fig. 5 | Visualization of the depth distribution of dendrites in SEs. a–g, Lithium concentration profiles in LiPON-25 °C (**a**), LLZO-25 °C (**b**), LLZO-60 °C (**c**), LLZO-100 °C (**d**), Li$_3$PS$_4$-25 °C (**e**), Li$_3$PS$_4$-60 °C (**f**) and Li$_3$PS$_4$-100 °C (**g**) at different times during lithium plating. The statement of uncertainty of these data is included in the Methods.

not help the dendrite suppression because the electronic conductivity of LLZO does not change much with the relative density (Supplementary Fig. 11). Whether the modification of grain boundaries can suppress dendrite formation really depends on if the electronic (not ionic) conductivity of the grain boundaries is decreased. Single-crystalline LLZO cannot prevent dendrite formation if its electronic conductivity is still high[57], although the critical potential of single-crystalline LLZO should be higher than that of polycrystalline LLZO because of the absence of free volume for dendrite formation. Achieving a better interfacial contact between Li and the SE by polishing the SE[25] or inserting an interlayer that could alloy with Li[20] can increase the 'apparent' critical current density due to an enlarged 'effective' contact area. However, because of the high electronic conductivity of the SE and the high electronic conductivity of the alloy interphase at the Li/SE

interface, the enlarged 'effective' contact area between Li and the SE could lower the potential in the SE, accelerating Li dendrite formation. In this regard, the formation of an ionically conducting, but electronically insulating interphase, the so-called SEI, between Li and SE is more desirable because the formation of the SEI could not only enlarge the 'effective' contact area but also lower the overall electronic conductivity of electrolytes (SE + SEI) and increase the potential in the bulk SE. The ultimate solution for dendrite suppression in the SE lies in lowering the electronic conductivity of the bulk electrolyte.

High ionic conductivity of > 10^{-4} S cm^{-1} has been considered a critical requirement for SEs[58]. However, there is no established constraint on the electronic conductivity. Our work demonstrates that low electronic conductivity should be another critical criterion for SEs regarding their practical application in lithium metal batteries.
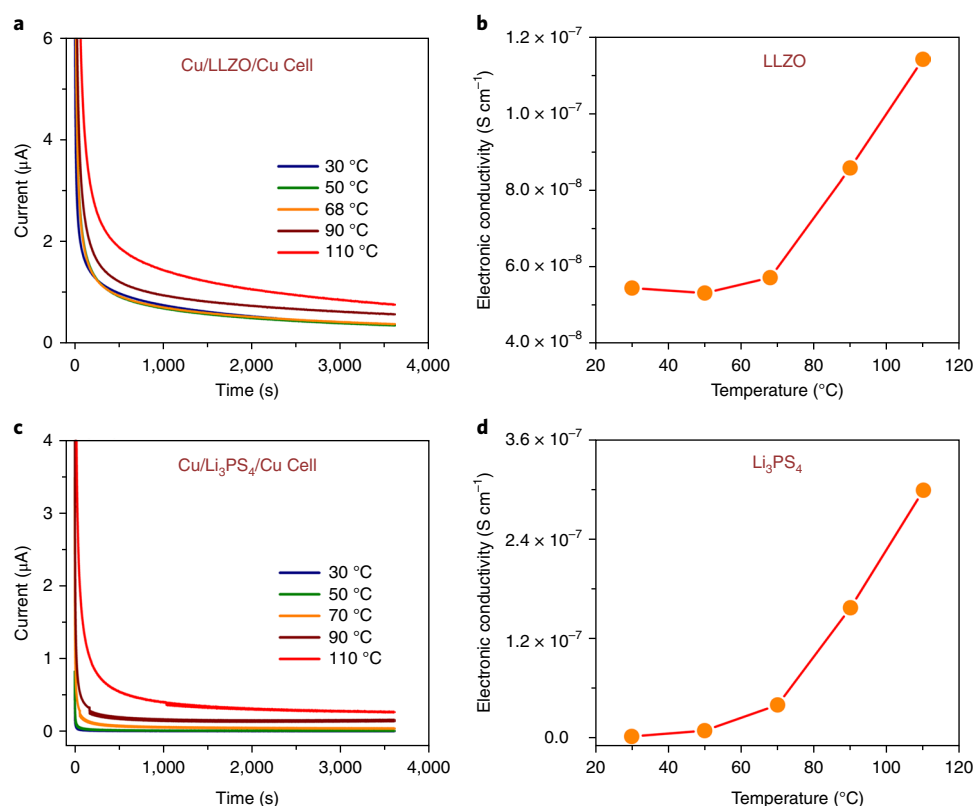
Fig. 6 | Temperature dependence of electronic conductivity. a,c, Current–time curves of the Cu/LLZO/Cu (**a**) and Cu/Li$_3$PS$_4$/Cu (**c**) cells under DC polarization at 100 mV. **b,d,** Electronic conductivities of LLZO (**b**) and Li$_3$PS$_4$ (**d**) at different temperatures.

The exact maximum value for the electronic conductivity is to be determined in future studies. Here we offer an empirical criterion on the basis of the correlation between the electronic conductivities and the critical current densities for three different SEs (LLZO, Li$_3$PS$_4$ and LiPON) (Supplementary Table 1). For a dendrite-free lithium plating at 1 and 10 mA cm^{-2}, the electronic conductivities of the SE should be lower than 10^{-10} and 10^{-12} S cm^{-1}, respectively.

In summary, we report the real-time visualization of lithium dendrite growth in LLZO and Li$_3$PS$_4$ SEs with operando NDP. The results suggest that lithium dendrites nucleate and grow directly inside LLZO and Li$_3$PS$_4$, and that high electronic conductivities of these materials are responsible for the dendrite formation in these SEs. This work highlights the critical role of lowering the electronic conductivity of SEs for dendrite-free Li plating at high current densities. Identifying the sources (for example, impurities, dopants, grain boundaries, or electrochemical reductions) for high electronic conductivity in LLZO and Li$_3$PS$_4$ SEs is therefore imperative. The electronic conductivity should be considered as another critical criterion for SEs for their application in all-solid-state lithium batteries.

Methods

Preparation of the LiCoO$_2$/LiPON/Cu cell. The LiCoO$_2$/LiPON/Cu thin-film cell was prepared following a previous report[10]. In sequence, 30 nm Co, 200 nm Pt, 3.1 μm LiCoO$_2$ cathode, 3.2 μm LiPON electrolyte, 200 nm Cu and a 700 nm LiPON overlayer were deposited on an alumina substrate. The area of the cell is around 0.5 cm^2. A thick LiCoO$_2$ cathode was used in the cell to provide a large amount of Li that can be plated on Cu. A thick LiPON electrolyte was used so that more information from the bulk region of the electrolyte could be measured. An additional LiPON overlayer was coated on top of the LiCoO$_2$/LiPON/Cu cell to protect the extruded Li from reacting with residual O$_2$ and H$_2$O in the vacuum chamber.

Preparation of the Li/LLZO/Cu cell. Ta-doped LLZO powder with a composition of Li$_{6.4}$La$_3$Zr$_{1.4}$Ta$_{0.6}$O$_{12}$ (LLZO) was prepared through a solid state reaction method

following previous work[43]. To prepare the LLZO electrolyte pellet, the as-obtained LLZO powders were pressed into pellets under a pressure of 120 MPa. The pellet was fully covered with the mother powder and sintered at 1,230 °C in air for 12 hours in an alumina crucible. The thickness and diameter of the LLZO pellet are around 1 mm and 1 cm^2, respectively. The top and bottom surfaces of the LLZO pellet were thouroughly polished inside an Ar-filled glovebox using sandpaper to complete remove the Li$_2$CO$_3$ and the Li-deficient layer on the LLZO surfaces. Then 200 nm Cu was deposited on the surface of LLZO using e-beam evaporation (Matra Thermal Evaporator at the Fablab of Univeristy of Maryland Nanocenter). The LLZO was exposed to the air for a few minutes during sample transfer for the e-beam deposition. The diameter of the Cu is 6 mm. The Li/LLZO/Cu cell was assembled by attaching a lithium disk (with a diameter of 8 mm and a thickness of 100 μm) on the other side of the LLZO pellet. The Li disk was scraped to remove the oxide layer on the surface. The Li/LLZO/Cu cell was assembled into a customized Al frame that was instrumented with a spring to maintain a certain stack pressure (~6.3 kPa) and an open window for the NDP measurement.

Preparation of the Li/Li$_3$PS$_4$/Pt cell. Amorphous Li$_3$PS$_4$ powder was synthesized by high-energy ball-milling Li$_2$S and P$_2$S$_5$ with a molar ratio of 3:1 at 510 r.p.m. for 60 hours (PM 100, Retsch). To prepare the Li/Li$_3$PS$_4$/Pt cell, 150 mg of the as-prepared Li$_3$PS$_4$ glass was pressed into a pellet under a pressure of 360 MPa. The thickness and diameter of the Li$_3$PS$_4$ pellet are around 1 mm and 1 cm, respectively. A thin layer of Pt (~300 nm) was sputtered on top of the pellet using a sputter coater (Cressington 108auto). The diameter of Pt is 8 mm. A 100-μm-thick Li metal with a diameter of 8 mm was attached on the other side of Li$_3$PS$_4$ pellet to make the Li/Li$_3$PS$_4$/Pt cell. The Li was scraped before attachment to the Li$_3$PS$_4$ pellet. The Li/Li$_3$PS$_4$/Pt cell was also assembled into a customized Al frame that was instrumented with a spring to maintain a certain stack pressure (~6.3 kPa) and an open window for the NDP measurement.

Characterization. The morphology of the sample was examined using a Hitachi SU-70 field-emission scanning electron microscope and a Hitachi NB-5000 dual (Focused Ion/Electron) beam microscope. The process of sample transfer is included in a previous report[59].

Electrochemistry. The charge (or discharge) process and the electrochemical impedance spectrum (EIS) measurement were performed on a potentiostat (BioLogic). The EIS was measured in the frequency range from 0.1 to 10^6 Hz after

resting at open-circuit potential for 30 minutes. The electronic conductivities of LLZO and Li_3PS_4 at different temperatures were measured by applying a 0.1 V DC voltage on the Cu/LLZO/Cu and Cu/Li_3PS_4/Cu cells.

NDP measurement. NDP spectra were acquired using a 'cold' neutron depth profiling facility (NG-5) at the NIST Center for Neutron Research (NCNR). The working principle is based on the nuclear reaction between ^6Li (natural lithium consists of ^6Li with a relative abundance of 7.5 at. %) and a neutron according to equation (1):

$$^6Li + n \rightarrow \ ^4He\,(2,055\ keV) + \ ^3H\,(2,727\ keV) \tag{1}$$
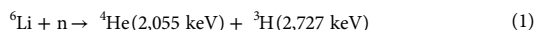
Emitted ^4He (α) and ^3H (triton) particles lose kinetic energy while travelling through the bulk medium of the specimen; hence the depth at which these particles form can be deduced from the final energy of the detected particles. Averaged typically over an area of a few square millimetres to more than 1 cm^2, NDP reveals Li depth profiles over a range of tens of micrometres with a depth resolution of a few tens of nanometres[49], depending on the atomic composition, mass density and sample geometry. Since the stopping power of α-particles is greater than that of tritons, the profiles for the LiCoO$_2$/LiPON/Cu thin-film cell are obtained using α-particle spectra that have higher depth resolution and provide more details, although both particles were detected. On the other hand, the weaker stopping power of tritons allow them to have larger penetration depth, which is desirable for profiling Li/LLZO/Cu and Li/Li_3PS_4/Pt cells with thick electrolytes. A 7.5-μm-thick Kapton film is placed on top of the Li/LLZO/Cu and Li/Li_3PS_4/Pt cells to eliminate interference of the α-particles in the triton spectrum. The NDP profiles of these cells were stored at three-minute intervals. A neutron monitor was also operated simultaneously with all measurements to correct for any minor fluctuations in the incoming neutron flux (~1% over a reactor cycle).

NDP data analysis. *Energy calibration.* An energy standard sample (LiNbO$_3$ crystal) was used to convert the channel number to energy of charged particles (*E*). The NDP spectrum of the standard is shown in Supplementary Fig. 1. Each detected charged particle has a specific energy based on equation (1). Since the energy of the charged particles is linearly associated with a channel number, their relationship can be established as equation (2):

$$E\,(keV) = 0.696 \times Channel + 38.267 \tag{2}$$

Depth calibration. The relationship between the detected energy (*E*) and the depth at which the charged particles were generated could be established using Stopping and Range of Ions in Matter (SRIM), from which the residual energy of the charged particles generated at different depths of the sample could be calculated. The compositions and densities of materials used for SRIM simulation are listed in Supplementary Table 2. It should be noted that the Kapton film is also included in the depth–energy simulation in SRIM. A second-order polynomial was used to fit the calculated results to get the analytical relationship between the detected energy and the depth (Supplementary Fig. 2), so that we were able to convert all 4,000 channels to depths. The interface between Cu (or Pt) and solid electrolytes (LiPON, LLZO and Li_3PS_4) is marked as the origin of the depth coordinate. Positive depth values encompass the thickness of the SEs.

The relationship between the detected energy of ^4He particles and their depth in the 700 nm LiPON + 200 nm Cu + 3.2 μm LiPON is determined to be

$$d\,(LiPON) = -3.654 \times 10^{-7} \times E^2 - 0.00207 \times E + 4.302 \tag{3}$$

The relationship between the detected energy of ^3H particles and their depth in the 7.5 μm Kapton film + 200 nm Cu + 1 mm LLZO is determined to be

$$d\,(LLZO) = -2.080 \times 10^{-7} \times E^2 - 0.00487 \times E + 22.013 \tag{4}$$

The relationship between the detected energy of ^3H particles and their depth in the 7.5 μm Kapton film + 300 nm Pt + 1 mm Li_3PS_4 is determined to be

$$d\,(Li_3PS_4) = -3.651 \times 10^{-6} \times E^2 - 0.00714 \times E + 39.598 \tag{5}$$

Note that the deposited Li and the Li build-up on the Cu (or Pt) were not considered in the depth calibration because for the LiCoO$_2$/LiPON/Cu cell, the total amount of Li transported to the anode is limited, and for the Li/LLZO/Cu and Li/Li_3PS_4/Pt cells, the stopping power of tritons in Li metal is very weak.

Concentration calibration. A ^{10}B-containing standard with a known area density ($D_{10B} = 1.094 \times 10^{16}$ atoms cm^{-2}) is used to convert the measured count rate to the Li concentration. The standard sample was measured in exactly the same geometrical setting as the in-situ electrochemical cell. This allows the areal density D_{Li} (atoms cm^{-2}) to be determined in the cells given the measured count rates of the standard (C_{10B}) and the sample (C_{6Li}), the cross-sections for the capture reaction of ^{10}B ($\sigma_{10B} = 3841.79$ barn) and ^6Li ($\sigma_{6Li} = 938.47$ barn) and the natural abundance of ^6Li ($A_{6Li} = 0.075$):

$$D_{Li}\,[atoms\ cm^{-2}] =$$
$$\frac{D_{10B}\,[atoms\ cm^{-2}] \times \sigma_{10B}\,[barn]}{A_{6Li} \times C_{10B}\,[counts\ s^{-1}] \times \sigma_{6Li}\,[barn]} \times C_{6Li}\,[counts\ s^{-1}] \tag{6}$$

To convert the areal density D_{Li} (atoms cm^{-2}) to the volumetric density D'_{Li} (atoms cm^{-3}), the area density is integrated every 10 channels and divided by the corresponding thickness covered by each 10 channels. The results are shown in Supplementary Fig. 3.

Statement of uncertainty. Possible sources of uncertainty within the NDP measurement include small-angle scattering of the charged particles, energy straggling of the particles, geometry (acceptance angle), measurement electronics (electronic noise, dead time), chemical composition of the sample, and the thickness of Kapton film. We believe the less than ideal counting statistics also contribute to the uncertainty of the results. Due to the transient nature of the in-situ measurement, the counting statics is relatively poor compared with the static measurement which could take a longer time for the data collection. As a result, we binned the counts of every 60–80 channels together to get the profiles shown in Fig. 5. The uncertainties from counting statistics (ε_C) can be estimated by $\sqrt{C}/C$, where *C* is the integrated counts for every 60–80 channels. The values of ε_C for LiPON, LLZO and Li_3PS_4 are determined to be < 5%, < 3%, and < 3%, respectively. We believe the error from background is negligible because no apparent change can be observed from the total counts for the same system tested at different temperatures. In addition, the statistical uncertainty in estimating the stopping power using SRIM is about 4%.

Data availability
The data that support the plots within this paper and other findings of this study are available from the corresponding author upon reasonable request.

References
1. Bruce, P. G., Freunberger, S. A., Hardwick, L. J. & Tarascon, J.-M. Li–O$_2$ and Li–S batteries with high energy storage. *Nat. Mater.* **11**, 19–29 (2012).
2. Harry, K. J., Hallinan, D. T., Parkinson, D. Y., MacDowell, A. A. & Balsara, N. P. Detection of subsurface structures underneath dendrites formed on cycled lithium metal electrodes. *Nat. Mater.* **13**, 69–73 (2014).
3. Tikekar, M. D., Choudhury, S., Tu, Z. & Archer, L. A. Design principles for electrolytes and interfaces for stable lithium-metal batteries. *Nat. Energy* **1**, 16114 (2016).
4. Albertus, P., Babinec, S., Litzelman, S. & Newman, A. Status and challenges in enabling the lithium metal electrode for high-energy and low-cost rechargeable batteries. *Nat. Energy* **3**, 16–21 (2018).
5. Janek, J. & Zeier, W. G. A solid future for battery development. *Nat. Energy* **1**, 16141 (2016).
6. Monroe, C. & Newman, J. The impact of elastic deformation on deposition kinetics at lithium/polymer interfaces. *J. Electrochem. Soc.* **152**, A396–A404 (2005).
7. Brissot, C., Rosso, M., Chazalviel, J. N. & Lascaud, S. Dendritic growth mechanisms in lithium/polymer cells. *J. Power Sources* **81**, 925–929 (1999).
8. Kerman, K., Luntz, A., Viswanathan, V., Chiang, Y. M. & Chen, Z. B. Review—practical challenges hindering the development of solid state Li ion batteries. *J. Electrochem. Soc.* **164**, A1731–A1744 (2017).
9. Bates, J., Dudney, N., Neudecker, B., Ueda, A. & Evans, C. Thin-film lithium and lithium-ion batteries. *Solid State Ionics* **135**, 33–45 (2000).
10. Neudecker, B. J., Dudney, N. J. & Bates, J. B. 'Lithium-free' thin-film battery with in situ plated Li anode. *J. Electrochem. Soc.* **147**, 517–523 (2000).
11. Kamaya, N. et al. A lithium superionic conductor. *Nat. Mater.* **10**, 682–686 (2011).
12. Kato, Y. et al. High-power all-solid-state batteries using sulfide superionic conductors. *Nat. Energy* **1**, 16030 (2016).
13. Murugan, R., Thangadurai, V. & Weppner, W. Fast lithium ion conduction in garnet-type Li$_7$La$_3$Zr$_2$O$_{12}$. *Angew. Chem. Int. Ed.* **46**, 7778–7781 (2007).
14. Sharafi, A., Meyer, H. M., Nanda, J., Wolfenstine, J. & Sakamoto, J. Characterizing the Li–Li$_7$La$_3$Zr$_2$O$_{12}$ interface stability and kinetics as a function of temperature and current density. *J. Power Sources* **302**, 135–139 (2016).
15. Ishiguro, K. et al. Ta-doped Li$_7$La$_3$Zr$_2$O$_{12}$ for water-stable lithium electrode of lithium–air batteries. *J. Electrochem. Soc.* **161**, A668–A674 (2014).
16. Sudo, R. et al. Interface behavior between garnet-type lithium-conducting solid electrolyte and lithium metal. *Solid State Ionics* **262**, 151–154 (2014).
17. Cheng, L. et al. Effect of surface microstructure on electrochemical performance of garnet solid electrolytes. *ACS Appl. Mater. Interfaces* **7**, 2073–2081 (2015).

18. Ren, Y. Y., Shen, Y., Lin, Y. H. & Nan, C. W. Direct observation of lithium dendrites inside garnet-type lithium-ion solid electrolyte. *Electrochem. Commun.* **57**, 27–30 (2015).

19. Schmidt, R. D. & Sakamoto, J. In-situ, non-destructive acoustic characterization of solid state electrolyte cells. *J. Power Sources* **324**, 126–133 (2016).

20. Tsai, C. L. et al. $Li_7La_3Zr_2O_{12}$ interface modification for Li dendrite prevention. *ACS Appl. Mater. Interfaces* **8**, 10617–10626 (2016).

21. Cheng, E. J., Sharafi, A. & Sakamoto, J. Intergranular Li metal propagation through polycrystalline $Li_{6.25}Al_{0.25}La_3Zr_2O_{12}$ ceramic electrolyte. *Electrochim. Acta* **223**, 85–91 (2017).

22. Yonemoto, F. et al. Temperature effects on cycling stability of Li plating/stripping on Ta-doped $Li_7La_3Zr_2O_{12}$. *J. Power Sources* **343**, 207–215 (2017).

23. Aguesse, F. et al. Investigating the dendritic growth during full cell cycling of garnet electrolyte in direct contact with Li metal. *ACS Appl. Mater. Interfaces* **9**, 3808–3816 (2017).

24. Sharafi, A., Haslam, C. G., Kerns, R. D., Wolfenstine, J. & Sakamoto, J. Controlling and correlating the effect of grain size with the mechanical and electrochemical properties of $Li_7La_3Zr_2O_{12}$ solid-state electrolyte. *J. Mater. Chem. A* **5**, 21491–21504 (2017).

25. Sharafi, A. et al. Surface chemistry mechanism of ultra-low interfacial resistance in the solid-state electrolyte $Li_7La_3Zr_2O_{12}$. *Chem. Mater.* **29**, 7961–7968 (2017).

26. Porz, L. et al. Mechanism of lithium metal penetration through inorganic solid electrolytes. *Adv. Energy Mater.* **7**, 1701003 (2017).

27. Garcia-Mendez, R., Mizuno, F., Zhang, R., Arthur, T. S. & Sakamoto, J. Effect of processing conditions of $75Li_2S–25P_2S_5$ solid electrolyte on its DC electrochemical behavior. *Electrochim. Acta* **237**, 144–151 (2017).

28. Han, F., Yue, J., Zhu, X. & Wang, C. Suppressing Li dendrite formation in $Li_2S–P_2S_5$ solid electrolyte by LiI incorporation. *Adv. Energy Mater.* **8**, 1703644 (2018).

29. Nagao, M. et al. In situ SEM study of a lithium deposition and dissolution mechanism in a bulk-type solid-state cell with a $Li_2S–P_2S_5$ solid electrolyte. *Phys. Chem. Chem. Phys.* **15**, 18600–18606 (2013).

30. Taylor, N. J. et al. Demonstration of high current densities and extended cycling in the garnet $Li_7La_3Zr_2O_{12}$ solid electrolyte. *J. Power Sources* **396**, 314–318 (2018).

31. Choudhury, S. & Archer, L. A. Lithium fluoride additives for stable cycling of lithium batteries at high current densities. *Adv. Electron. Mater.* **2**, 1500246 (2016).

32. Qian, J. et al. High rate and stable cycling of lithium metal anode. *Nat. Commun.* **6**, 6362 (2015).

33. Raj, R. & Wolfenstine, J. Current limit diagrams for dendrite formation in solid-state electrolytes for Li-ion batteries. *J. Power Sources* **343**, 119–126 (2017).

34. Yu, S. et al. Elastic properties of the solid electrolyte $Li_7La_3Zr_2O_{12}$ (LLZO). *Chem. Mater.* **28**, 197–206 (2016).

35. Iriyama, Y., Kako, T., Yada, C., Abe, T. & Ogumi, Z. Charge transfer reaction at the lithium phosphorus oxynitride glass electrolyte/lithium cobalt oxide thin film interface. *Solid State Ionics* **176**, 2371–2376 (2005).

36. Chen, Y.-T. et al. Voltammetric enhancement of Li-ion conduction in Al-doped $Li_{7−x}La_3Zr_2O_{12}$ solid electrolyte. *J. Phys. Chem. C* **121**, 15565–15573 (2017).

37. Rangasamy, E., Wolfenstine, J. & Sakamoto, J. The role of Al and Li concentration on the formation of cubic garnet solid electrolyte of nominal composition $Li_7La_3Zr_2O_{12}$. *Solid State Ionics* **206**, 28–32 (2012).

38. Shin, B. R. et al. Comparative study of TiS_2/Li–In all-solid-state lithium batteries using glass-ceramic Li_3PS_4 and $Li_{10}GeP_2S_{12}$ solid electrolytes. *Electrochim. Acta* **146**, 395–402 (2014).

39. Minami, K., Mizuno, F., Hayashi, A. & Tatsumisago, M. Lithium ion conductivity of the $Li_2S–P_2S_5$ glass-based electrolytes prepared by the melt quenching method. *Solid State Ionics* **178**, 837–841 (2007).

40. Li, J., Dudney, N. J., Nanda, J. & Liang, C. Artificial solid electrolyte interphase to address the electrochemical degradation of silicon electrodes. *ACS Appl. Mater. Interfaces* **6**, 10083–10088 (2014).

41. Le Van-Jodin, L., Ducroquet, F., Sabary, F. & Chevalier, I. Dielectric properties, conductivity and Li^+ ion motion in LiPON thin films. *Solid State Ionics* **253**, 151–156 (2013).

42. Su, Y. et al. LiPON thin films with high nitrogen content for application in lithium batteries and electrochromic devices prepared by RF magnetron sputtering. *Solid State Ionics* **282**, 63–69 (2015).

43. Han, F. D., Zhu, Y. Z., He, X. F., Mo, Y. F. & Wang, C. S. Electrochemical stability of $Li_{10}GeP_2S_{12}$ and $Li_7La_3Zr_2O_{12}$ solid electrolytes. *Adv. Energy Mater.* **6**, 1501590 (2016).

44. De Jonghe, L. C., Feldman, L. & Beuchele, A. Slow degradation and electron conduction in sodium/beta-aluminas. *J. Mater. Sci.* **16**, 780–786 (1981).

45. De Jonghe, L. C. Transport number gradients and solid electrolyte degradation. *J. Electrochem. Soc.* **129**, 752–755 (1982).

46. Liu, Z. et al. Interfacial study on solid electrolyte interphase at Li metal anode: Implication for Li dendrite growth. *J. Electrochem. Soc.* **163**, A592–A598 (2016).

47. Peled, E. The electrochemical behavior of alkali and alkaline earth metals in nonaqueous battery systems—the solid electrolyte interphase model. *J. Electrochem. Soc.* **126**, 2047–2051 (1979).

48. Ziegler, J. F., Baglin, J. E. E. & Cole, G. W. Technique for determining concentration profiles of boron impurities in substrates. *J. Appl. Phys.* **43**, 3809–3815 (1972).

49. Downing, R. G., Lamaze, G. P., Langland, J. K. & Hwang, S. T. Neutron depth profiling: Overview and description of NIST facilities. *J. Res. Natl Inst. Stand. Technol.* **98**, 109–126 (1993).

50. Gao, J., Shi, S.-Q. & Li, H. Brief overview of electrochemical potential in lithium ion batteries. *Chin. Phys. B* **25**, 018210 (2015).

51. Zhou, W. et al. Plating a dendrite-free lithium anode with a polymer/ceramic/polymer sandwich electrolyte. *J. Am. Chem. Soc.* **138**, 9385–9388 (2016).

52. Luntz, A. C., Voss, J. & Reuter, K. Interfacial challenges in solid-state Li ion batteries. *J. Phys. Chem. Lett.* **6**, 4599–4604 (2015).

53. Kim, K. H. et al. Characterization of grain-boundary phases in $Li_7La_3Zr_2O_{12}$ solid electrolytes. *Mater. Charact.* **91**, 101–106 (2014).

54. Cheng, L. et al. Effect of microstructure and surface impurity segregation on the electrical and electrochemical properties of dense Al-substituted $Li_7La_3Zr_2O_{12}$. *J. Mater. Chem. A* **2**, 172–181 (2014).

55. Aryanfar, A. et al. Thermal relaxation of lithium dendrites. *Phys. Chem. Chem. Phys.* **17**, 8000–8005 (2015).

56. Aryanfar, A. et al. Annealing kinetics of electrodeposited lithium dendrites. *J. Chem. Phys.* **143**, 134701 (2015).

57. Kataoka, K., Nagata, H. & Akimoto, J. Lithium-ion conducting oxide single crystal as solid electrolyte for advanced lithium battery application. *Sci. Rep.* **8**, 9965 (2018).

58. Schnell, J. et al. All-solid-state lithium-ion and lithium metal batteries—paving the way to large-scale production. *J. Power Sources* **382**, 160–175 (2018).

59. Ma, C. et al. Interfacial stability of Li metal–solid electrolyte elucidated via in situ electron microscopy. *Nano. Lett.* **16**, 7030–7036 (2016).

Author contributions

F.H. performed the operando NDP tests, analysed the data and wrote the manuscript. A.S.W. and N.J.D. fabricated the $LiCoO_2/LiPON/Cu$ thin-film cells and were intimately involved in the manuscript writing. J.Y. fabricated the Li/LLZO/Cu and $Li/Li_3PS_4/Pt$ cells and helped with the electrochemical testing. X.F. and F.W. performed the SEM tests of the LLZO and Li_3PS_4 pellets after Li plating. M.C. and D.N.L. performed the FIB-SEM test. H.W. advised on the NDP test and data analysis. C.W. supervised the study and contributed to the manuscript writing. All authors discussed the results.

Competing interests

The authors declare no competing interests.

Additional information

Supplementary information is available for this paper at https://doi.org/10.1038/s41560-018-0312-z.

Reprints and permissions information is available at www.nature.com/reprints.

Correspondence and requests for materials should be addressed to N.J.D. or H.W. or C.W.

Publisher's note: Springer Nature remains neutral with regard to jurisdictional claims in published maps and institutional affiliations.